• Original Paper •

Multiscale Combined Action and Disturbance Characteristics of Pre-summer Extreme Precipitation Events over South China※

Hongbo LIU[*1], Ruojing YAN[1,2], Bin WANG[1,2], Guanghua CHEN[3], Jian LING[1], and Shenming FU[4]

[1]*State Key Laboratory of Numerical Modeling for Atmospheric Sciences and Geophysical Fluid Dynamics (LASG),*
Institute of Atmospheric Physics, *Chinese Academy of Sciences*, *Beijing* 100029, *China*

[2]*College of Earth and Planetary Sciences*, *University of Chinese Academy of Sciences*, *Beijing* 100049, *China*

[3]*Key Laboratory of Cloud-Precipitation Physics and Severe Storms (LACS)*, *Institute of Atmospheric Physics*,
Chinese Academy of Sciences, *Beijing* 100029, *China*

[4]*International Center for Climate and Environment Sciences (ICCES)*, *Institute of Atmospheric Physics*,
Chinese Academy of Sciences, *Beijing* 100029, *China*

ABSTRACT

The dominant frequency modes of pre-summer extreme precipitation events (EPEs) over South China (SC) between 1998 and 2018 were investigated. The 67 identified EPEs were all characterized by the 3–8-d (synoptic) frequency band. However, multiscale combined modes of the synoptic and three low-frequency bands [10–20-d (quasi-biweekly, QBW); 15–40-d (quasi-monthly, QM); and 20–60-d (intraseasonal)] accounted for the majority (63%) of the EPEs, and the precipitation intensity on the peak wet day was larger than that of the single synoptic mode. It was found that EPEs form within strong southwesterly anomalous flows characterized by either lower-level cyclonic circulation over SC or a deep trough over eastern China. Bandpass-filtered disturbances revealed the direct precipitating systems and their life cycles. Synoptic-scale disturbances are dominated by mid–high latitude troughs, and the cyclonic anomalies originate from downstream of the Tibetan Plateau (TP). Given the warm and moist climate state, synoptic-scale northeasterly flows can even induce EPEs. At the QBW and QM scales, the disturbances originate from the tropical Pacific, downstream of the TP, or mid–high latitudes (QBW only). Each is characterized by cyclonic–anticyclonic wave trains and intense southwesterly flows between them within a region of large horizontal pressure gradient. The intraseasonal disturbances are confined to tropical regions and influence SC by marginal southwesterly flows. It is concluded that low-frequency disturbances provide favorable background conditions for EPEs over SC and synoptic-scale disturbances ultimately induce EPEs on the peak wet days. Both should be simultaneously considered for EPE predictions over SC.

Key words: extreme precipitation event, dominant frequency band, multiscale combined action, disturbance characteristics, South China

Article Highlights:

- Pre-summer EPEs over SC are all characterized by falling within the 3–8-d synoptic-scale frequency band.
- Multiscale combined actions between synoptic and low-frequency disturbances dominate EPEs and enhance the precipitation intensity.
- The mid–high latitudes, downstream of the TP, and tropical western Pacific are three major areas of origin for different scale disturbances.

---

1. Introduction

South China (SC) is the rainiest region of the Chinese mainland. The pre-summer rainy season over SC usually refers to 1 April to 30 June and is characterized by large quantities of cumulative rainfall (>800 mm in northern Guangxi

and central and southern Guangdong) (Luo et al., 2017) and the frequent occurrence of extreme precipitation events (EPEs) lasting from several hours to several days (Bao, 2007; Huang et al., 2019; Miao et al., 2019). SC occupies a special geographical location in which it is exposed to the simultaneous influences of both mid–high-latitude and tropical–subtropical weather systems. Its long coastline, complex topography and large metropolises further complicate the formation mechanisms of EPEs (Du et al., 2020a, b; Yin et al., 2020); plus, extremely persistent heavy precipitation tends to occur near land–sea boundaries and mountainous areas (Zhang et al., 2021). With the continuous progression of urbanization, the frequency of extreme precipitation (shorter than 1 day) has tended to increase during the past several decades (Wu et al., 2019). In addition, SC is home to the highest frequency of persistent extreme rainfall events in the broader region of central and eastern China, with a particular increase in frequency since 1990 that has often led to regional flooding events in the warm season (Chen and Zhai, 2013). Hence, SC is a region with a high risk of flooding, along with related losses of life and property, meaning extreme precipitation and related research has emerged as a hot topic in recent years (Luo et al., 2020).

Precipitation in the warm season over SC shows obvious low-frequency oscillation signals, which can be partly attributed to the influence of disturbances from the mid–high-latitude or tropical–subtropical regions (Li and Zhou, 2015; Miao et al., 2019). The low-frequency oscillation activities affecting both the South China Sea (SCS) and SC consist of two major mode—namely, 20–60-d intraseasonal oscillation (ISO) and 10–20-d quasi-biweekly (QBW) oscillation (Mao and Chan, 2005; Zhou and Chan, 2005; Hong and Ren, 2013; Pan et al., 2013; Li et al., 2015; Wang and Zhang, 2019). In terms of precipitation, QBW oscillation is the predominant low-frequency mode over SC (Tang et al., 2007; Gu et al., 2013; Pan et al., 2013). In the pre-summer rainy season, the low-level circulation accompanied by heavy rainfall exhibits a cyclonic anomaly over SC and an anticyclonic anomaly over the SCS (Hong and Ren, 2013). The cyclonic anomaly is believed to originate from mid–high latitudes, and propagates southeastwards within a cyclonic–anticyclonic Rossby wave pattern (Tang et al., 2007; Pan et al., 2013). Two QBW low-frequency upper-level wave trains have been identified—one crossing the Eurasian continent and the other along the subtropical westerly jet. The wave energy disperses eastwards along the wave trains and it enhances the relative vorticity of the cyclonic anomaly over eastern China, which further intensifies the ascending motion over SC before triggering persistent heavy rainfall (Miao et al., 2019). The anticyclonic anomaly over the SCS usually reflects the westward extension of the western Pacific subtropical high (WPSH). Its cause is attributable either to the northwestward propagation of the tropical–subtropical QBW wave train or the southwestward propagation of the anticyclonic anomaly from SC before the precipitation occurs (Chen and Sui, 2010; Cao et al., 2012;

Hong and Ren, 2013). The intense southwesterly perturbation between the cyclonic and anticyclonic anomalies ensures a continuous water vapor supply from the Bay of Bengal (BOB), SCS and western Pacific, thus helping to maintain the persistent precipitation over SC (Liu et al., 2016).

High-frequency synoptic-scale disturbances also play vital roles in regional EPEs; for example, five continuous synoptic-scale disturbances resulted in flash flooding in the Huaihe River Basin in summer 2003 (Liu et al., 2014). It has been found that 3–8 d is the dominant frequency mode at the synoptic scale for regional EPEs in SC (Huang et al., 2018). These precipitating synoptic-scale disturbances mainly exhibit cyclonic or trough-type anomalies, which originate from downstream of the Tibetan Plateau (TP) or can be traced back to the mid-latitude Rossby wave train.

In fact, heavy precipitation may be simultaneously affected by multiscale disturbances. Li and Zhou (2015) analyzed the multiscale control of summertime (July–September) heavy precipitation events in terms of both synoptic and intraseasonal time scales. Enhanced convection, a continuously huge water vapor supply, and subsequent persistent heavy precipitation were found to be the synergistic result of interacting ISO (defined as 10–90-d in their paper) and synoptic-scale disturbances; however, when the two systems are asynchronous, the precipitation intensity is typically weaker. It should be noted, however, that the analysis did not distinguish the exact frequency bands involved in certain rainfall cases, but rather simply separated the 10–90-d ISO components into 30–60-d Madden–Julian oscillation (MJO) and QBW modes. Jiang et al. (2020) further explored the multiscale effects on pre-summer heavy rainfall episodes and revealed that, in addition to the combined action of synoptic and QBW disturbances, synoptic and quasi-monthly (15–40-d, QM) disturbances were also prominent in 2009 and 2013. The QM band is not a remarkable frequency mode of ISO and has rarely been studied, but it did regulate the large-scale circulation that led to heavy precipitation over the middle and lower Yangtze River Basin in summer 1991 (Mao and Wu, 2006).

Warm season heavy rainfall over SC is an indisputable result of interactions among other high-frequency (< 3 days) multiscale systems, such as the synoptic system-related low-level jet, and mesoscale phenomena including the boundary layer jet, land–sea breeze, urban heat island effects, and cold pools, as well as the coastline, terrain, land use, etc. (Chen et al., 2016; Jiang et al., 2017; Du and Chen, 2019a, b; Huang et al., 2019; Yin et al., 2020; Gao et al., 2021). In contrast, there is no comprehensive understanding of the effect of the combined action of these disturbances on extreme precipitation in much larger and longer-term systems. As introduced above, the influence of low-frequency ISO circulation anomalies on heavy precipitation events over SC has been extensively and well investigated, and the role of synoptic-scale disturbances has also been confirmed. However, whether it is a universal truth that pre-summer EPEs over SC are jointly controlled by synoptic and ISO dis-

turbances, as in the case studies presented by Jiang et al. (2020), remains an open question. Besides, if it is true, what are the relative proportions of single synoptic-scale and multiscale disturbances associated with EPEs, and what is the dominant low-frequency band modulating the multiscale EPEs? These issues will be addressed in this paper. In addition, because Li and Zhou (2015) focused on summer (July–September), both synoptic and ISO disturbances all originated from the tropical regions and propagated northwestwards; whereas, mid–high latitudes weather systems are quite active in the pre-summer rainy season (Pan et al., 2013; Huang et al., 2018). Therefore, another objective of this study is to clarify the circulation configuration characteristics, including the area of origin and life cycle of different scale disturbances, as well as their relative contributions to EPEs.

Following this introduction, the next section describes the data and methods used in this study. Section 3 presents the climatology of pre-summer precipitation during 1998–2018, the distribution of extreme precipitation in each year, and the corresponding frequency bands of EPEs. In section 4, bandpass-filtered anomalous circulation patterns are classified and analyzed based on single or multiscale combined actions, and the relative contribution of each component is further shown in the multiscale combined modes. The final section gives a summary of the results and provides a schematic diagram of the major areas of origin and propagation pathways of disturbances at each time scale.

2. Data and methods

2.1. Data

Three sets of precipitation data were used in this study. The first is the Daily Surface Observations in China dataset (V3.0), which comprises in-situ observations provided by the China Meteorological Data Service Centre. It begins from the year 1951 and includes roughly 839 stations across the Chinese mainland since 1998.

The second dataset is the research-quality daily TRMM (Tropical Rainfall Measurement Mission) Multi-Satellite Precipitation Analysis (TMPA, 3B42) provided by NASA's Goddard Space Flight Center (Huffman et al., 2016). TMPA incorporates both microwave and infrared estimates of precipitation, as well as monthly rain gauge precipitation products for adjustment (Huffman and Bolvin, 2018). Its spatial resolution is 0.25° × 0.25° latitude/longitude and covers the domain of 50°N–50°S because microwave and infrared estimates tend to lose skill at higher latitudes (Huffman et al., 2010).

The third data source is NOAA's Climate Prediction Center (CPC) morphing technique (CMORPH) dataset. CMORPH adopts a different approach, independent of that of TMPA. It takes advantage of the high quality of passive microwave data, as well as the high spatial and temporal resolution of infrared data. Here, the infrared dataset was employed to derive a cloud motion field that was used to prop-

agate raining pixels, and therefore only the passive microwave–derived precipitation estimates in CMORPH were used (Joyce et al., 2004). The raw CMORPH data have a spatial resolution of ~0.10° latitude × 0.10° longitude and cover a spatial domain of 60°N–60°S at a 30-min temporal resolution. Both the daily CMORPH with corrected bias (CMORPH-CRT) and satellite-gauge blended CMORPH (CMORPH-BLD) products were used, each with spatial resolutions of 0.25° × 0.25°. In CMORPH-CRT, a probability density function bias correction method was adopted to reduce the bias of raw CMOPRH precipitation over land against CPC daily rain gauge analysis data, and over ocean against Global Precipitation Climatology Program pentad merged precipitation analysis data (Xie et al., 2017). CMORPH-BLD, meanwhile, a satellite–gauge blended product, was obtained by merging CMORPH-CRT and CPC daily rain gauge analysis data using an optimal interpolation technique (Chen et al., 2008).

Daily mean data from ERA-Interim—a global atmospheric reanalysis dataset produced by ECMWF (Dee et al., 2011)—were used to depict the large-scale circulation patterns associated with SC EPEs. The horizontal resolution of this dataset is 1.5° and its vertical resolutions are 25 hPa between 1000 and 750 hPa, 50 hPa between 750 and 250 hPa, and 25 hPa between 250 and 100 hPa.

All the data used in this study covered the period from 1 January 1998 to 31 December 2018 (a total of 21 years). The precipitation related to typhoons or tropical cyclones that occurred over SC were eliminated from our analysis by manual screening.

2.2. Methods

The procedure used to select single-scale or multiscale EPEs was as follows: First, an EPE was defined as a rainfall case in which the daily precipitation rate over the core region of SC (defined in section 3) exceeded the 95th percentile (about 3 standard deviations) of the daily rainfall series from April to June during 1998–2018. It was found that the numbers of consistent extreme rainy days (above 95th percentile) may vary from 1 to 3 (there was only 1 case that the consecutive extreme rainy days reached 4 days). Therefore, if the precipitation intensity of two or three consecutive days reached the extreme precipitation standard, it was considered as one EPE.

Second, to obtain the dominant frequency bands of precipitation in the pre-summer rainy season, a year-by-year power spectrum analysis was carried out for the daily rainfall series averaged over the core region. The statistical significance of the power spectra was tested based on the Markov red-noise spectrum (Liu et al., 2014). Here, a log parameter is defined as the ratio between variance of computed rainfall power spectrum and variance of corresponding Markov rednoise spectrum, which is called "log ratio". When the log ratio is equal or larger than 0.0, the power spectra signal is significant.

Third, after determining the major precipitation frequency band, bandpass filtering based on the fast Fourier

transform method was applied to the anomalous precipitation series (the annual cycle was removed by subtracting the 21-year daily climatology). If the bandpass-filtered precipitation anomaly on peak wet phase (the largest positive rainfall anomaly day) reached or exceeded one standard deviation of the corresponding filtered rainfall anomalies, the EPE was determined to be significant at this time scale [similar criteria were also adopted by Yang et al. (2010) and Gao et al. (2018)]. In general, positive precipitation anomaly peaks at the synoptic scale closely matched the rainfall peak of EPE (i.e., the heaviest rainy day). But for the oscillations longer than 10 days, the above two peaks may not coincide with each other. To ensure the sample numbers and highlight the effects of low-frequency oscillations on EPEs, 1–2 days shift between the two peaks was allowed. If an EPE is significant at one time scale (both synoptic and low-frequency time scales), the single-scale (multiscale) EPE was identified. Periodic fluctuations in precipitation and circulation fields were also extracted using fixed-period bandpass filtering at each grid point to analyze the origin and propagation characteristics of the disturbances.

Both objective and subjective classification methods were tested for the circulation anomaly fields related to the single and multiscale combined action of EPEs. Multivariate empirical orthogonal function (MV_EOF) analysis (Wang, 1992) was used to capture the dominant patterns of bandpass-filtered precipitation and associated circulation anomalies over SC on peak precipitation days. Then, the composite fields of each type showed the origin and propagation vector of precipitating disturbances. Due to the fewer samples of multiscale EPEs, as well as the large variety of sources and wide spatial range of low-frequency oscillation, MV_EOF is unsuitable for the classification of low-frequency disturbances. Therefore, in this study, MV_EOF analysis was only applied to synoptic-scale EPEs.

The detailed steps are as follows: (1) the April–June precipitation and the 850-hPa zonal and meridional wind anomaly series (determined by removing the three components' climatological values) during the period 1998–2018 were respectively linked into a long-term time series, which was then considered as the input for the MV_EOF analysis; (2) MV_EOF analysis was performed to obtain the leading EOF modes and associated principal component (PC) time series; (3) upon comparing the PC values of each leading mode with the raw precipitation series, the MV_EOF mode with the largest PC value on peak precipitation days of EPEs was selected as the prominent EPE disturbance pattern; (4) the MV_EOF decomposition fields were reconstructed into physical fields and compared with bandpass-filtered fields—if they were similar, this MV_EOF mode was accepted; and (5) having classified the bandpass-filtered fields based on steps (3) and (4), composite analysis was then adopted for each type of bandpass-filtered anomalous circulation field from phase 1 to phase 5 to reveal the precipitating systems.

As for the low-frequency disturbances of the multiscale combined mode, subjective classification was carried out by focusing on the tracks of the EPE-related anomalous circulation systems in each phase.

3. Major frequency modes of EPEs

During the pre-summer rainy season, the precipitation intensity increases gradually over SC from April to June; it is about 3–9 mm d^{-1} in April, 7–13 mm d^{-1} in May, and 9–15 mm d^{-1} in June (Fig. 1). The four precipitation datasets show a very similar distribution in each month, and TMPA 3B42 has the highest spatial correlation coefficients with STN in each month (0.95, 0.89, 0.90; Table 1). Specifically, there are two major precipitation centers in SC that are located in northern Guangxi Province and over the southeast coast–northern Pearl River Delta, respectively. According to the spatial distribution of daily mean precipitation in each month over SC, the area with large values (21°–26°N, 108°–117°E) was selected as the core region in this study. It should be mentioned that the relatively large area means that some locally occurring warm-sector extreme rainfall events were excluded in our study. These cases always happen suddenly and are usually characterized by complicated boundary layer triggering mechanisms, complex topography, land–sea thermal contrasts, and especially, weaker synoptic scale baroclinic forcing (He et al. 2016). Based on the 95th percentile of daily precipitation series (rainy days), the criteria of EPEs for the station, TMPA, CMORPH-CRT and CMORPH-BLD data are 27.0, 28.0, 24.0 and 24.0 mm d^{-1}, respectively (Table 2). Following the methods described in section 2.2, year-by-year pre-summer rainy season precipitation power spectra averaged over SC were computed for the four datasets (figures not shown). Four dominant frequency bands were identified in the 21-year study period—namely, 3–8 d, 10–20 d, 15–40 d, and 20–60 d. As an intuitive example, Fig. 2 integrates the power spectra and period distributions of the TMPA data for all 21 years. Clearly, the 3–8-d high-frequency synoptic mode is the most significant period in each of the 21 years, followed by the QBW, ISO and QM modes. Moreover, the results were qualitatively consistent when the other three datasets were used (not shown).

Apart from the highest spatial correlation coefficients between TMPA 3B42 and STN in each month, it is apparent that the EPE criterion and one standard deviation of bandpass-filtered precipitation at the synoptic and QBW scales of TMPA are quite similar to those of the station observations (with differences of 0.1–0.2 mm d^{-1}), but the values of CMORPH-CRT and CMORPH-BLD are obviously underestimated (with differences of 0.2–0.6 mm d^{-1}) (Table 2). In addition, CMORPH-CRT and CMORPH-BLD show low (discontinuous) precipitation areas near the Pearl River Delta (Figs. 1g–l), which was also found in Huang et al. (2018) and noted by other Chinese scientists (personal communication). Considering the above two factors, the CMORPH data are not analyzed further. The TMPA precipitation is highly consistent with that of the station observations over
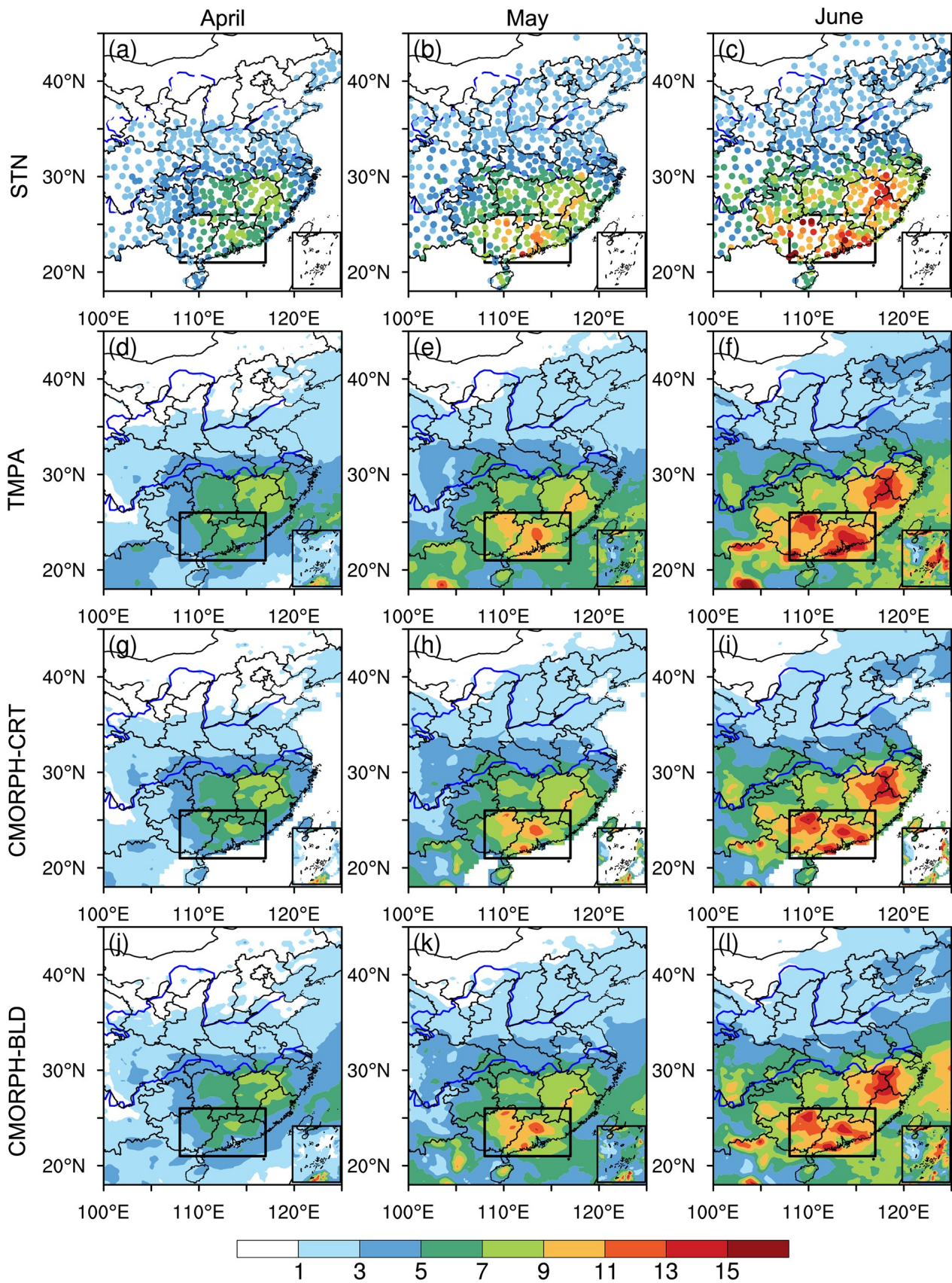
Fig. 1. Spatial distribution of the temporally averaged station, TMPA 3B42, CMORPH-CRT and CMORPH-BLD daily precipitation rates (mm d^{-1}) over China for (a, d, g, j) April, (b, e, h, k) May, and (c, f, i, l) June of 1998–2018. The inset box denotes the core region of SC (21°–26°N, 108°–117°E), which is the same in subsequent figures.

the Chinese mainland and covers the ocean surface where EPEs often happen. Therefore, only the TMPA data are

employed in the remainder of the paper.

Based on the spectral peaks (i.e., the filled values equal to or greater than 0.0 in Fig. 2) of precipitation in each year, bandpass-filtered precipitation anomalies and raw precipitation time series were compared to select EPEs and corresponding dominant frequency modes (Fig. 3). Here, the extreme rainfall days associated with tropical cyclones are excluded (e.g., three cases in 2018). To ensure the reliability of the analysis, the heavy rainfall should also exist in the other three datasets on the same day. EPE activity exhibits obvious inter-annual variations, e.g., six cases in 1998 and none in 2017 and 2018 (two EPEs in June were affected by typhoons),

Table 1. The spatial correlation coefficients (significant at 99% Student's *t*-test) between monthly averaged rainfall of STN and TMPA 3B42, CMORPH-CRT, CMORPH-BLD for 63 stations over SC. The grid datasets are interpolated to stations.

Datasets	April	May	June
TMPA 3B42 vs. STN	0.95	0.89	0.90
CMORPH-CRT vs. STN	0.80	0.71	0.64
CMORPH-BLD vs. STN	0.90	0.79	0.79

Table 2. EPE thresholds and one standard deviation of bandpass-filtered precipitation (mm d^{-1}) in each frequency band for the four datasets over the core region of SC.

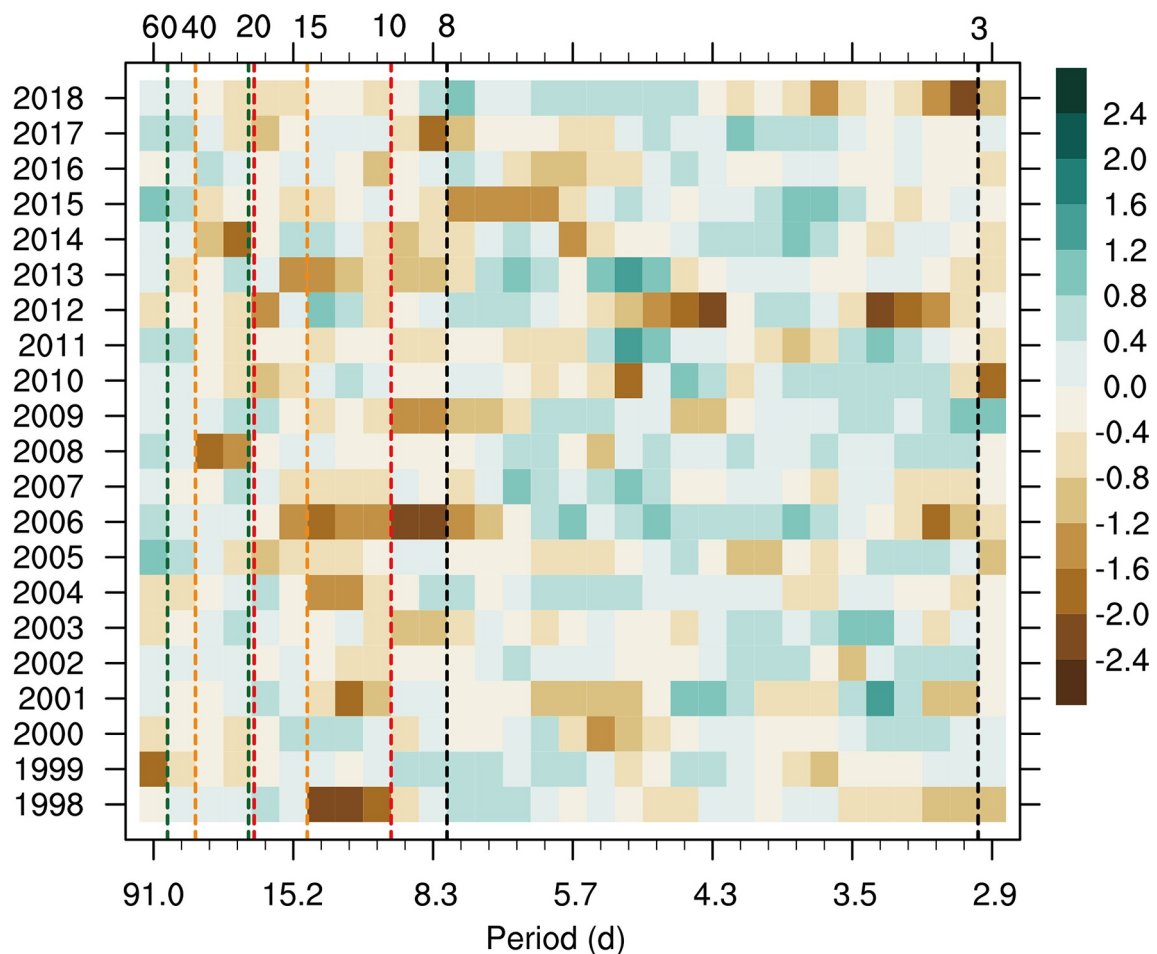| Dataset	EPE	Synoptic (3–8-d)	QBW (10–20-d)	QM (15–40-d)	ISO (20–60-d)
STN	27.0	5.4	3.6	3.4	3.1
TMPA 3B42	28.0	5.3	3.8	3.7	3.4
CMORPH-CRT	24.0	4.8	3.4	3.3	3.0
CMORPH-BLD	24.0	4.9	3.4	3.2	3.0

Fig. 2. The year-by-year distribution of the pre-summer rainy season precipitation power spectra averaged over SC during 1998–2018. The filled values are log values of the computed power spectrum divided by the corresponding Markov red-noise spectrum (log values equal to or larger than 0.0 mean that the computed spectrum is significant). The abscissa is period in days. The four dominant frequency bands are indicated by the dashed lines with different colors.
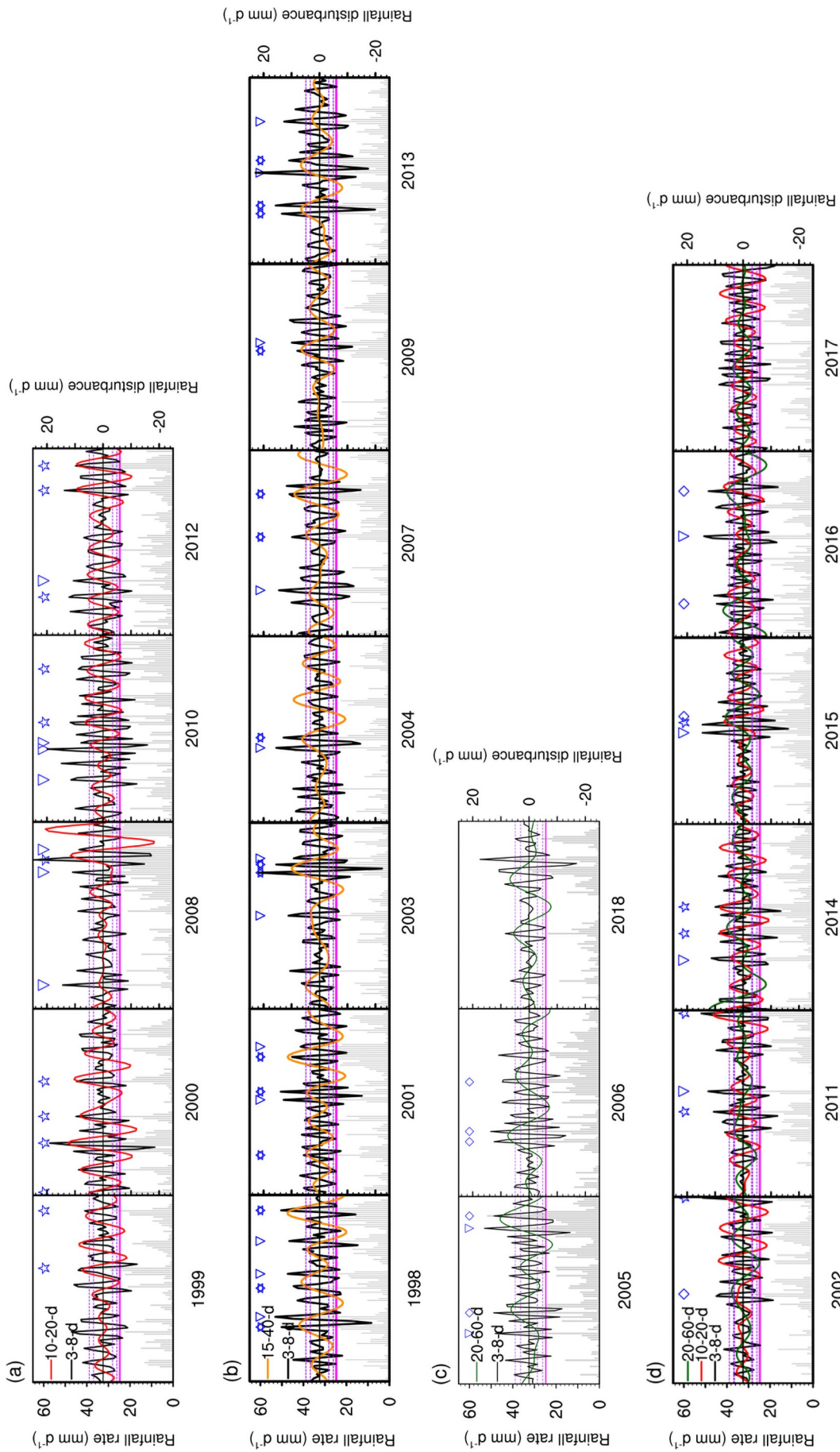
Fig. 3. Time series of raw daily precipitation rates (gray bars; mm d⁻¹; left y-axis), bandpass-filtered precipitation anomalies (red: 10–20-d; orange: 15–40-d; green: 20–60-d; black: 3–8-d; mm d⁻¹; right y-axis) during the period 1 April to 30 June 1998–2018. The x axis represents time period of April to June in each year. The years are classified into four groups based on the dominant frequency bands in each year: (a) 3–8-d, 10–20-d, (b) 3–8-d, 15–40-d; (c) 3–8-d, 20–60-d; (d) 3–8-d, 10–20-d and 20–60-d. Solid pink lines represent the extreme precipitation intensity over SC; dashed pink lines represent one standard deviation of bandpass-filtered precipitation in each frequency band. The symbols ▽, ☆, ✿, ◇ and ◇ represent EPEs accompanied by significant 3–8-d, 3–8-d & 10–20-d, 3–8-d & 15–40-d, and 3–8-d & 20–60-d disturbances, respectively.

Table 3. The 67 significant EPEs classified by dominant frequency modes for the TMPA 3B42 dataset. The dates refer to the peak precipitation day.

Synoptic	Synoptic&QBW	Synoptic&QM	Synoptic&ISO
19980502	19990526	19980427	20020514
19980523	19990623	19980516	20050505
19980608	20000402	19980623	20050621
20010517	20000426	20010420	20060427
20010612	20000509	20010521	20060502
20030516	20000526	20010607	20060526
20030613	20020630	20030606	20150523
20040507	20080612	20030610	20160417
20050425	20100519	20040512	20160611
20050615	20100614	20070519	–
20070423	20110512	20070609	–
20080412	20110629	20090519	–
20080606	20120419	20130425	–
20080617	20120610	20130429	–
20090523	20120622	20130521	–
20100421	20140508	–	–
20100506	20140521	–	–
20100509	20150520	–	–
20110522	–	–	–
20120427	–	–	–
20130515	–	–	–
20130609	–	–	–
20140425	–	–	–
20150515	–	–	–
20160520	–	–	–

with three to four cases occurring in most years (Table 3, Fig. 3). We find that EPEs are most active in May and less active in April. In the pre-summer seasons of the 21-year study period, there are a total of 67 EPEs, and each EPE has one (synoptic) or two (synoptic and QBW/QM/ISO) dominant frequency modes (Tables 3 and 4). Among them, the 3–8-d single synoptic mode has the largest number (25) of cases (37%). However, the case numbers for the 3–8-d & 10–20-d, 3–8-d & 15–40-d, and 3–8-d & 20–60-d multiscale combined modes are far higher than the single synoptic modes. In addition to holding the majority in terms of numbers, the peak precipitation intensities of the multiscale combined modes are also somewhat larger (~36.0 mm d⁻¹) than those of the single synoptic modes (33.5 mm d⁻¹) (Table 4). Figure 4 presents the composite results for four types of EPEs. The peak precipitation days coincide well with the peaks of each bandpass-filtered positive rainfall anomaly. As in Liu et al. (2014), the phase analysis method was adopted to identify the life cycle of each EPE, as well as the spatial structures and temporal evolution of the precipitating disturbances. The peak dry phase (phase 1, P1) and peak wet phase (phase 5, P5) refer to the minimum and maximum precipitation day at each time scale, respectively (Fig. 4). Obviously, the precipitation intensity on peak wet days is far more intense than on other days in all four EPE types.

Based on the raw circulation fields, EPEs over SC are all accompanied by intense cyclonic or trough-type systems in the lower troposphere (relative to the climatology), and the heavy precipitation is mainly located at the front of these systems where strong southwesterly moisture flux converges and upward motion takes place (Fig. 5). The BOB, SCS and western Pacific are three major water vapor source regions for EPEs over SC. Specifically, the southwesterly flow anomalies are strongest in the 3–8-d & 20–60-d multiscale combined mode, which transport vast amounts of warm, moist air from the BOB to SC (Fig. 5d). In addition, the northerly anomalies behind the deep mid–high-latitude trough also enhance the intrusion of cold air mass. In the 3–8-d and 3–8-d & 10–20-d modes, the spatial range of the WPSH is more similar to that of the climatology (Figs. 5a and b). A slight eastward retreat and broad westward extension of the WPSH (compared to the respective climatology) happens for the 3–8-d & 15–40-d and 3–8-d & 20–60-d multiscale combined modes, respectively. Despite the slight eastward retreat of the WPSH, a lower-level anomalous high-pressure system exists in the northern Philippines, and the enhanced pressure gradient strengthens the southwesterly flow along the coastal region over SC (Fig. 5c). In comparison, the high-pressure system in the 3–8-d & 20–60-d combined mode is deep and wide, and its western flank even covers the Indochina Peninsula. The strong and stable WPSH ensures a steady stream of moisture supply from the BOB to SC (confirmed by whole column integrated water vapor flux anomalies, not shown). At 200 hPa, the westerly jet core in the 3–8-d & 15–40-d combined mode moves eastwards compared to the climatology (110°E vs 95°E). Because SC is located on the south side of the westerly jet entrance area, it corresponds to a region of upper-level divergence associated with the jet transverse circulation (Ding, 2005), which induces upward motion and therefore strengthens low-level convergence and the subsequent precipitation

Table 4. The EPE cases (percentage) and the peak precipitation intensity (mm d⁻¹) in each type of dominant frequency mode for the TMPA 3B42 dataset in the pre-summer rainy season during 1998–2018.

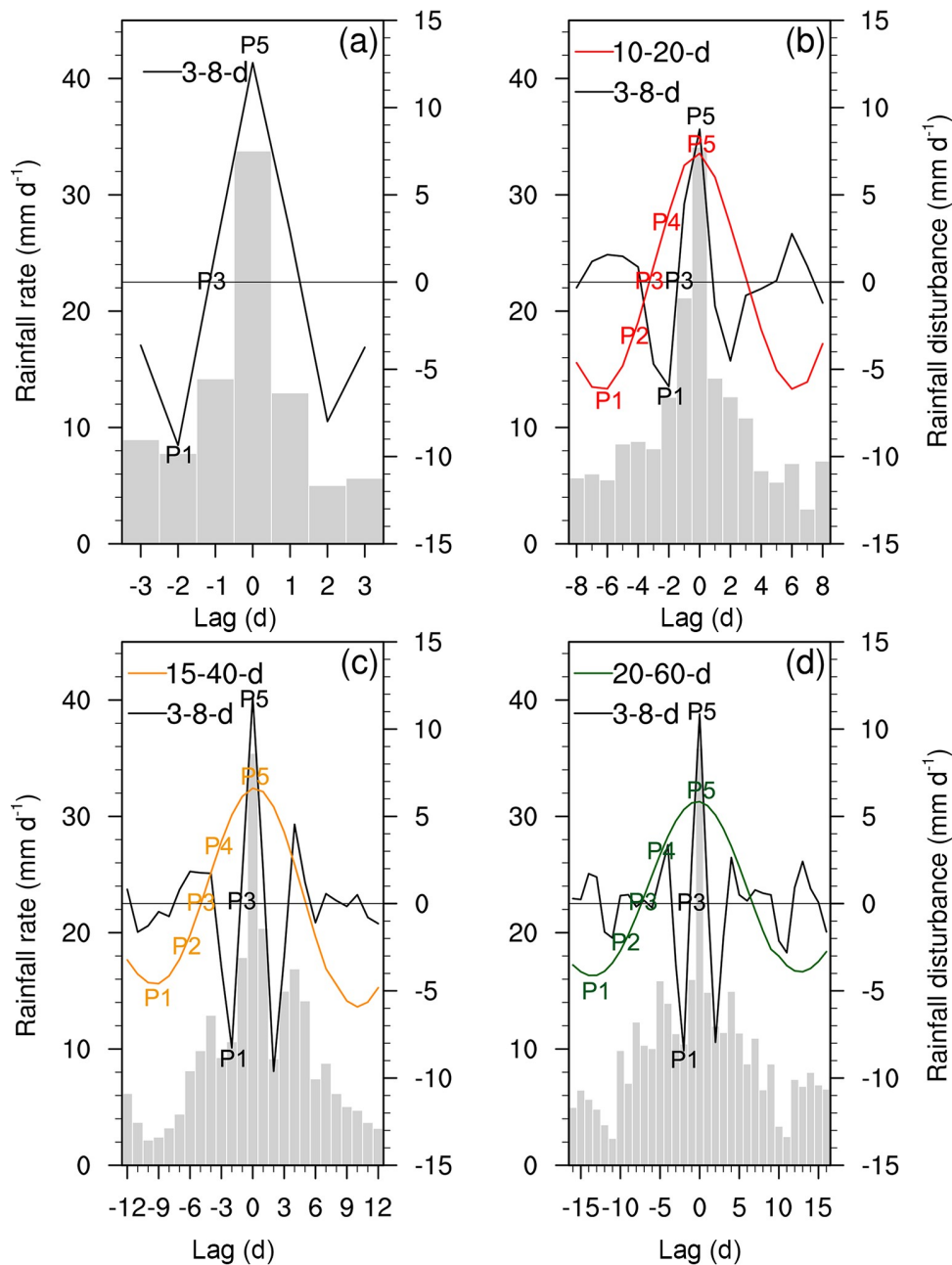| Dominant frequency mode/modes	EPE Cases (percentage)	Peak precipitation intensity (mm d⁻¹)
Synoptic	25 (37%)	33.5
Synoptic&QBW	18 (27%)	36.6
Synoptic&QM	15 (22%)	36.4
Synoptic&ISO	9 (14%)	35.8
No significant bands	–	–

Fig. 4. Composite of four types of EPEs at the (a) synoptic, (b) synoptic & QBW, (c) synoptic & QM, and (d) synoptic & ISO time scale. P1 and P5 refer to the peak dry and peak wet day on each time scale, and P2 to P4 are the middle phases. The gray bars, black line, red line, orange line and green line refer to the composite raw precipitation (left *y*-axis), and 3–8-d, 10–20-d, 15–40-d and 20–60-d bandpass-filtered precipitation anomalies (right *y*-axis), respectively. The *x*-axis refers to the exact precipitation day relative to the peak wet day (0).

intensity over SC.

Clearly, the raw fields in each EPE type exhibit quite diverse circulation characteristics. Hence, the precipitating disturbances at both the high-frequency synoptic scale and the synoptic with low-frequency QBW, QM and ISO combined modes should be respectively analyzed to better understand the formation processes and mechanisms of SC EPEs. In the next section, we focus on exploring different scale disturbances.

4. Disturbance classification and characteristic analysis

4.1. *3–8-d synoptic-scale disturbances*

As analyzed in section 3, despite the majority of the 67 identified EPEs being multiscale combined actions, each is accompanied by a typical synoptic-scale mode. Therefore, synoptic-scale disturbances are analyzed first. It has been
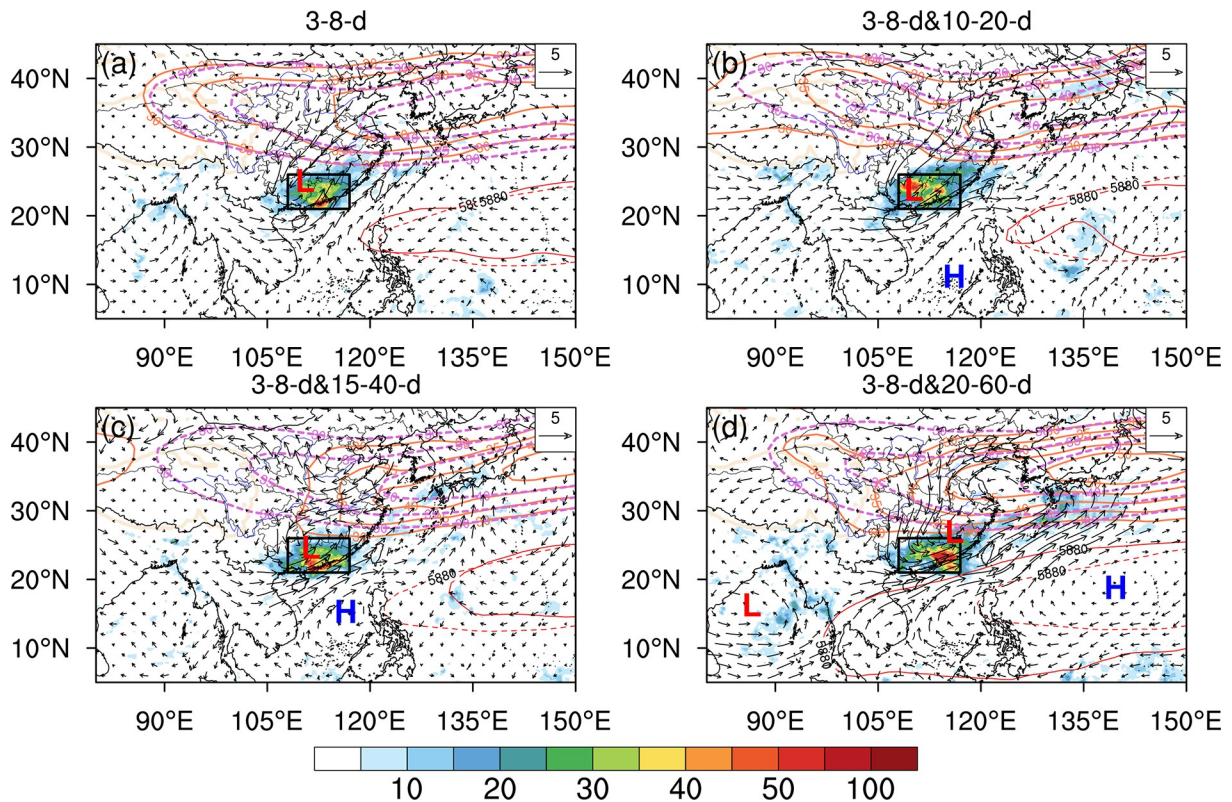
Fig. 5. Composite fields of daily precipitation rate anomalies (mm d^{-1}; shaded; relative to climatology) and 850-hPa wind vector anomalies (m s^{-1}), 500-hPa 5880-m geopotential isoline (red solid line) and climatology (red dashed lines), and 200-hPa total wind speed (30 m s^{-1}; orange solid lines) and climatology (pink dashed lines) for the EPEs associated with (a) 3–8-d, (b) 3–8 & 10–20-d, (c) 3–8 & 15–40-d and (d) 3–8 & 20–60-d disturbances. The climatologies here all refer to the composite of specific peak precipitation days. The letters "L" and "H" denote anomalous low- and high-pressure systems.

found that EPE-related systems are most prominent in the lower troposphere, and the influence of synoptic-scale disturbances is relatively small (Liu et al., 2014; Zhang et al., 2017; Huang et al., 2018). Based on MV_EOF analysis, four types of typical synoptic-scale disturbances were identified: mid–high latitude troughs (18 cases; type I), Yangtze–Huaihe cyclones (17 cases; type II), SC cyclones (13 cases; type III), and Yellow–Huaihe anticyclones (8 cases; type IV) (Fig. 6). The precipitating disturbances in the other 11 cases were hard to identify and are therefore not discussed.

In type I, negative precipitation and anticyclonic circulation anomalies control SC in phase 1, with the mid–high-latitude trough appearing north of 35°N (Fig. 6a). Then, the trough deepens and marches rapidly southwards (Fig. 6b). In phase 5, the northerly flows behind the trough guide the cold air southwards to SC, and a large positive precipitation anomaly becomes located at the bottom of the trough (Fig. 6c).

The precipitating cyclonic anomalies in types II and III both originate from downstream of the TP and propagate northeastwards or southeastwards as cyclonic–anticyclonic wave trains, respectively (Figs. 6d–f, Figs. 6g–i). In type II, positive precipitation anomalies occupy the southeast quadrant of the cyclonic anomaly, where the powerful southwest-

erly flow transports vast amounts of water vapor from the SCS and converges over SC. In contrast, the positive precipitation anomaly always occurs with the cyclonic anomaly from phase 1 in type III. Both cyclonic and precipitation anomalies strengthen as they propagate southeastwards and reach their peak in phase 5. Despite the relatively small spatial scale of the cyclonic anomaly and weak southerly in type III, it is the positive relative vorticity and strong moisture convergence that lead to EPEs in this type.

The last type has the fewest cases, in which the anticyclonic–cyclonic wave train originates from mid–high latitudes and propagates southeastwards. Different from the other three types, it is the northeasterly anomaly with relatively cold, dry air masses that influences SC, and intense positive precipitation anomalies only appear in phase 5, which concentrate along the southeast coastal region. This type of synoptic-scale disturbance is quite similar to that described by Liu et al. (2014), who found that warm, moist background conditions along with cold, dry northeasterly flow can also trigger EPEs. In the multiscale combined action modes, the synoptic-scale disturbances show random distributions of the four types (including atypical cases).

Overall, in pre-summer rainy season, the identified EPE at the synoptic time scale are dominated by the westerly weather systems. The synoptic-scale disturbance classifica-
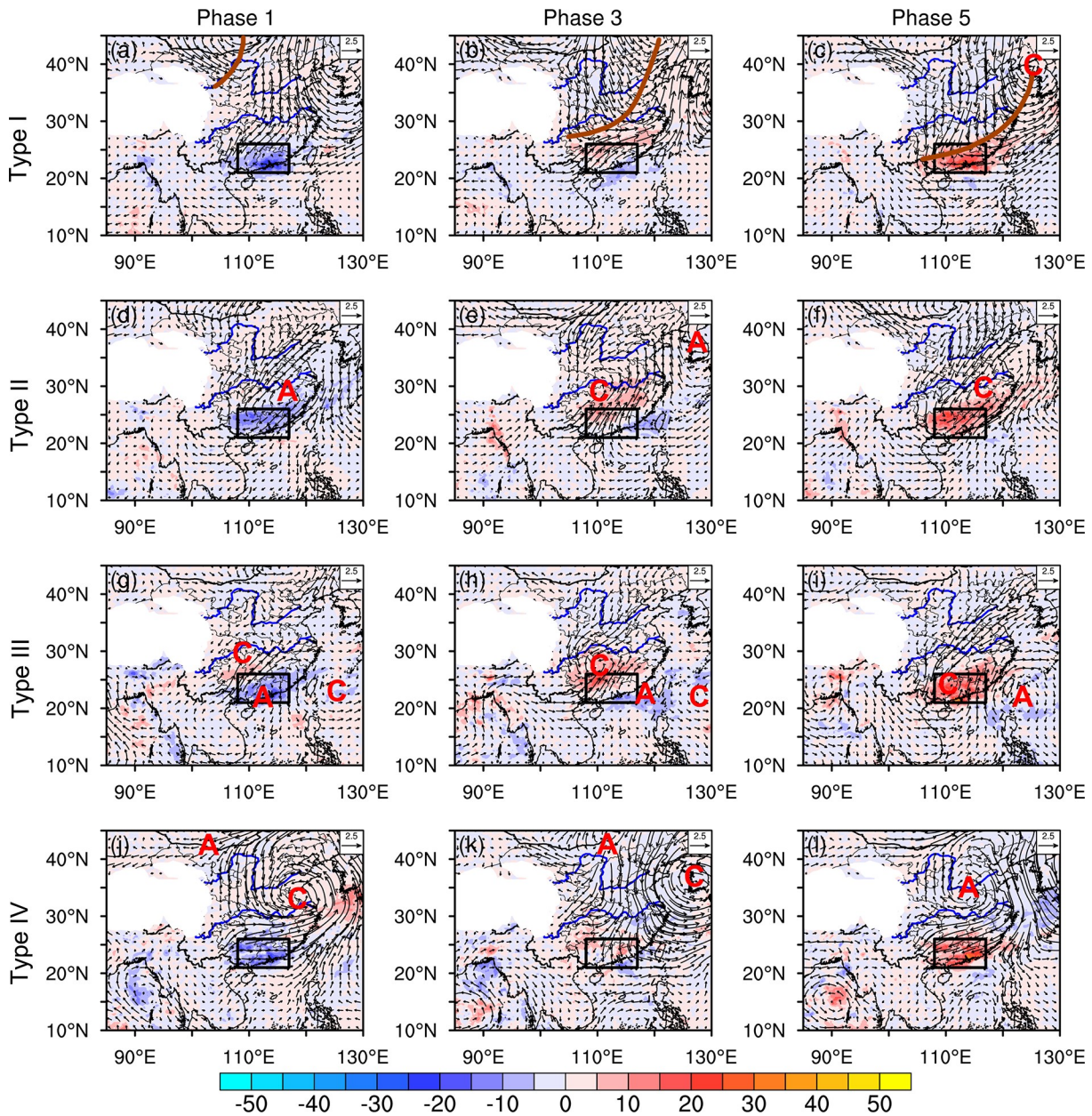
Fig. 6. Temporal evolution of the 3–8-d bandpass-filtered 850-hPa daily mean wind anomalies (m s^{-1}) and daily precipitation rate anomalies (shaded, mm d^{-1}) for the four types of synoptic-scale disturbances from phase 1 to phase 5. The thick brown curve denotes the trough. The letters "C" and "A" denote cyclonic and anticyclonic circulation anomalies, respectively. Similar conventions apply for the following figures.

tion results in this study are qualitatively consistent with those of Huang et al. (2018), despite the adoption of different precipitation datasets and classification methods (objective vs subjective). It is certain that there are precipitating disturbances from the subtropical ocean area (e.g., SCS) at the synoptic scale, but the number of cases is very limited.

4.2. *Low-frequency disturbances in the multiscale combined modes*

Low-frequency disturbances are characterized by a longer life history and wider spatial range, which provide more favorable circulation background conditions for EPEs. The subjective classification in this study focuses on the pre-

cipitating system on the peak wet day, and then traces backwards to the peak dry day.

Three types of QBW disturbances are distinguished: tropical western Pacific wave trains (type I; 6 cases), extended troughs of the mid–high-latitude cyclonic anomaly (type II; 4 cases), and wave trains downstream of the TP (type III; 4 cases) (Fig. 7). Clearly, the scopes of QBW disturbance activity are wider, ranging from mid–high-latitude to tropical regions, and maintain roughly the same proportion. The anomalous cyclonic–anticyclonic wave train originating from the tropical western Pacific in type I is a typical QBW disturbance that usually affects EPEs or heat waves in eastern
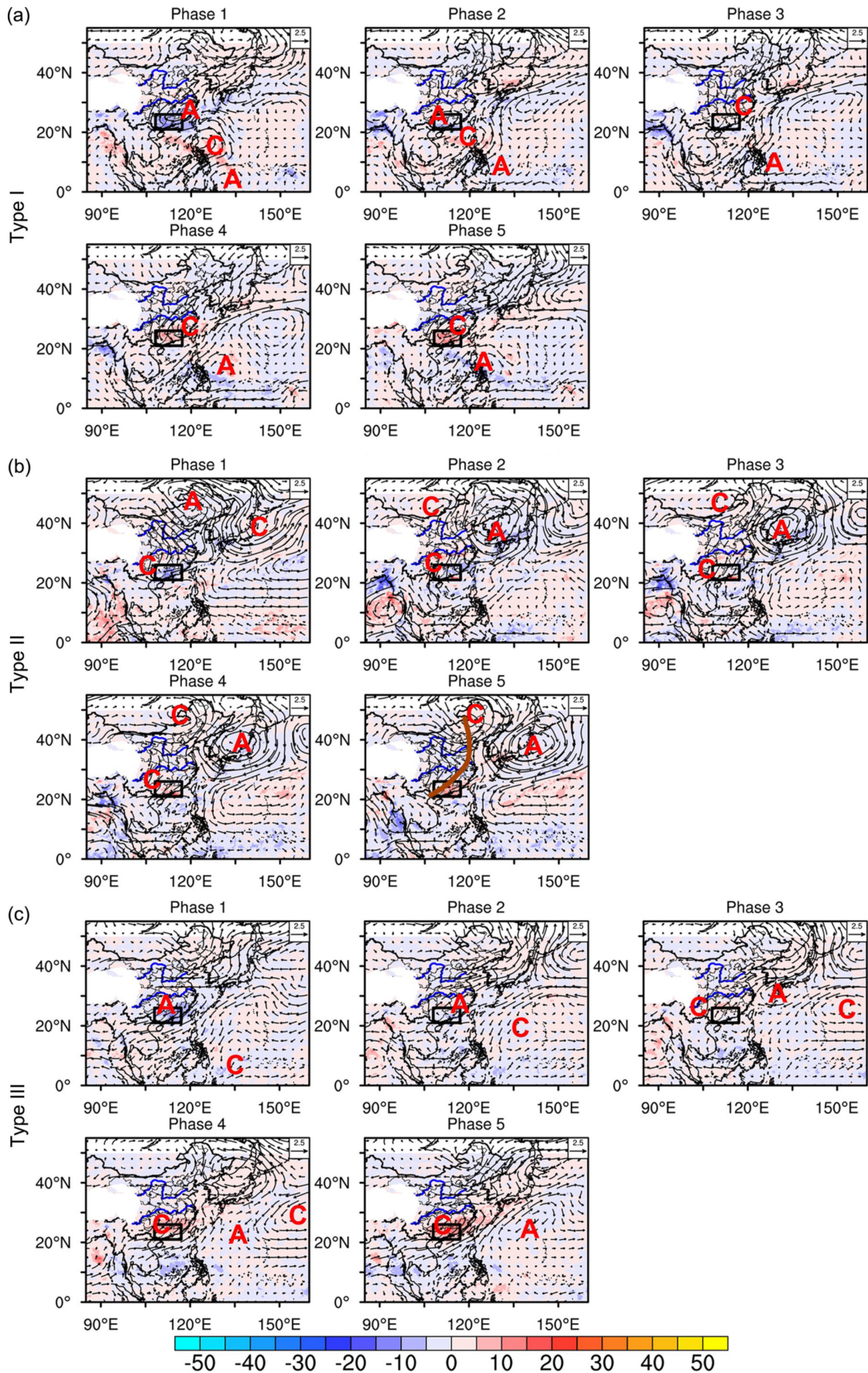
Fig. 7. As in Fig. 6 but for the 10–20-d bandpass-filtered disturbances and precipitation anomalies.

China (Liu et al., 2014; Li and Zhou, 2015; Gao et al., 2018). The wave train propagates continuously northwestwards, and the cyclonic anomaly becomes stable over SC in phase 3 before then strengthening with increasing precipitation until reaching its peak in phase 5 (Fig. 7a). In type II, the mid–high-latitude wave train and cyclonic anomaly east of the TP propagate synchronously eastwards and ultimately evolve into the extended trough of the mid–high-latitude cyclonic anomaly on the peak wet day (Fig. 7b). This type of QBW disturbance is quite similar to the low-frequency wave train along the subtropical westerly jet found in Miao et al. (2019). In type III, the coupled cyclonic–anticyclonic anomalies originate from downstream of the TP and then propagate eastwards to the northwestern Pacific (Fig. 7c). The positive precipitation anomaly increases with the strengthening and convergence of the southwesterly flow in front of the cyclonic anomaly from phase 3 to phase 5.

The two types of QM disturbances are quite like the 1st- and 3rd-type QBW disturbances, except that the coupled cyclonic–anticyclonic anomalies propagate southeastwards to the SCS in type II (Fig. 8). The intense southwesterly perturbation between the cyclonic–anticyclonic anomaly couplet is the key component for EPEs. Despite the WPSH not showing any westward expansion, an 850-hPa high-pressure system still exists in the raw field on the peak wet day (Fig. 5c). Bandpass filtering reveals that this high-pressure system is
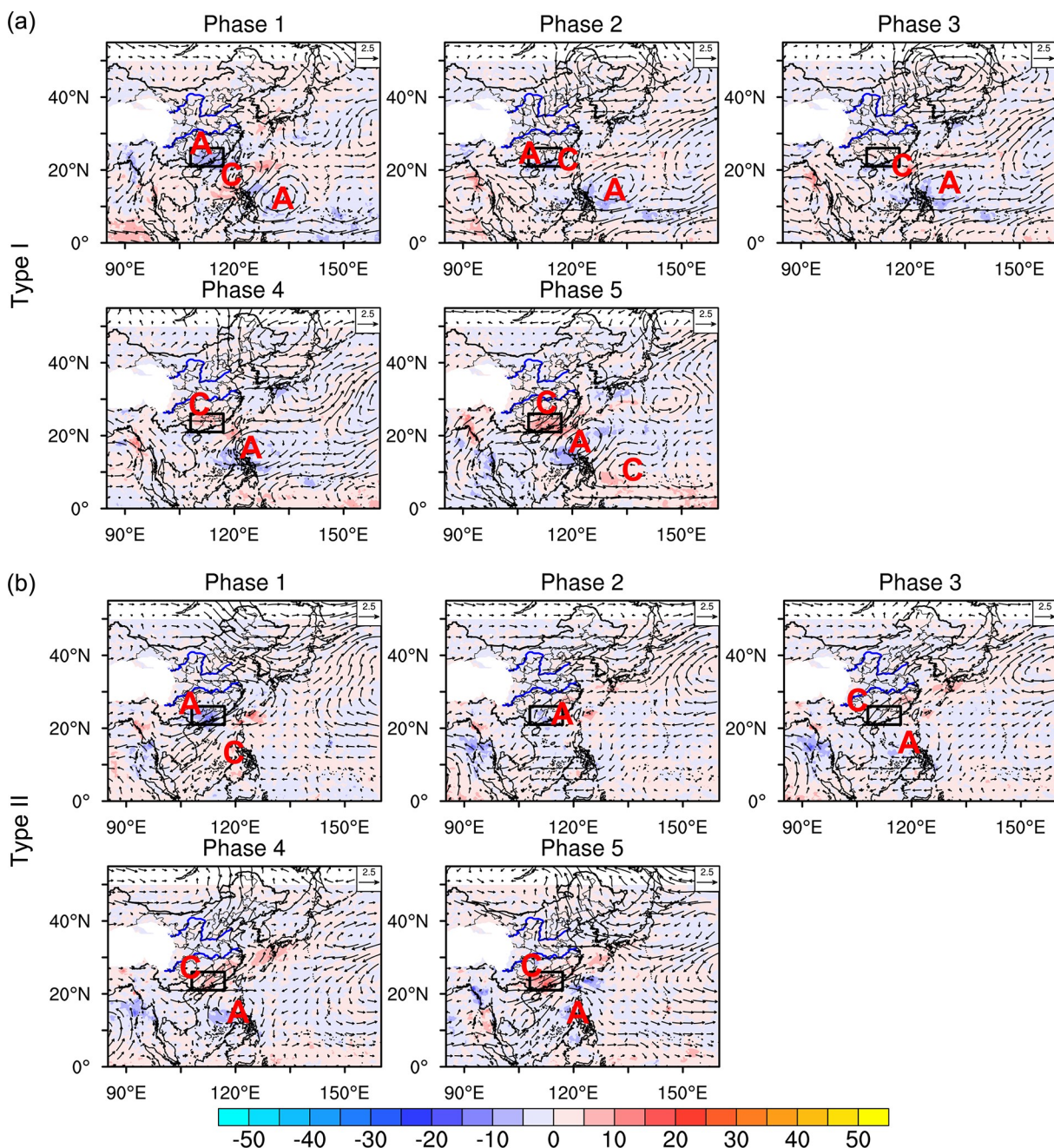

Fig. 8. As in Fig. 6 but for the 15–40-d bandpass-filtered disturbances and precipitation anomalies.

the result of the low-level QM-scale anticyclonic anomaly in the northern Philippines, which can be traced to the eastern Philippines or downstream of the TP (Fig. 8). Combined with the findings in Jiang et al. (2020), it can be concluded that the strong southwesterly anomaly is the most critical component for EPEs at the QM scale.

At the ISO scale of the 3–8-d & 20–60-d combined mode, there is no direct precipitating disturbance over SC as there is at the other three time scales. The most prominent signals are the westward propagation of the tropical cyclonic and anticyclonic anomalies south of 20°N (Fig. 9). In phase 1, a cyclonic anomaly with two closed centers exists over the SCS and the western Pacific, respectively, and SC is controlled by a northeasterly anomaly with a negative precipitation anomaly. An anticyclonic anomaly simultaneously exists in the tropical Pacific. In phase 2, the cyclonic anomaly with two centers propagates westwards to the eastern BOB and SCS, and the anticyclonic anomaly strengthens and moves westwards. Then, the cyclonic anomaly over the SCS disappears and the anticyclonic anomaly expands further in phase 3. In phases 4 and 5, the cyclonic anomaly propagates to the northern BOB and the anticyclonic anomaly continues to expand and splits into two centers, which are exactly the same as the two centers of the cyclonic anomaly in phase 1. From phase 4, the southwesterly anomaly between the cyclonic–anticyclonic couplet stretches from the BOB to SC, and the abundant water vapor supply and moisture convergence lead to a positive precipitation anomaly over SC. Both the southwesterly anomaly and precipitation over SC reach their peak in phase 5. The bandpass-filtered cyclonic–anticyclonic anomaly couplet is stable and powerful, which is also apparent in the raw field as indicated by

the 850-hPa low/high pressure couplet over the BOB and western Pacific (cf. Fig. 9e and Fig. 5d). Although EPEs with the 3–8-d & 20–60-d combined mode can happen in April, May or June, the area of origin and propagation pathway of the bandpass-filtered disturbances are robust, which means the 20–60-d ISO signal may provide early signs for the prediction of heavy precipitation over the SC region.

4.3. *Combined action of multiscale disturbances*

Abundant water vapor supply and continuous moisture convergence are the key components for large-scale regional extreme precipitation episodes (Wang et al., 2016; Ding, 2019; Tabari, 2020). In order to reveal the relative contributions/actions of the synoptic-scale and three low-frequency disturbances, the variable most related to precipitation was analyzed. Specifically, the area-averaged 1000–300-hPa vertically integrated moisture flux convergence (VIMFC) over SC was computed and then corresponding bandpass filtering was performed on it to extract the VIMFC disturbance at each time scale. The peak wet day is denoted as day 0, and then variables are traced back to day −3.

For all three multiscale combined modes, the synoptic-scale VIMFC exhibits divergence over SC on day −3 and day −2 (Table 5). From day −1, the synoptic-scale VIMFC becomes convergent and reaches its peak on day 0. On the three low-frequency time scales (QBW, QM and ISO), the VIMFCs are all convergent, with the values gradually increasing and maximizing on day −1 or day 0. In fact, day −3 roughly corresponds to phase 4 of the QBW, QM and ISO modes, which all form a quite favorable cyclonic anomaly or intense southwesterly convergence pattern (Figs. 7–9).
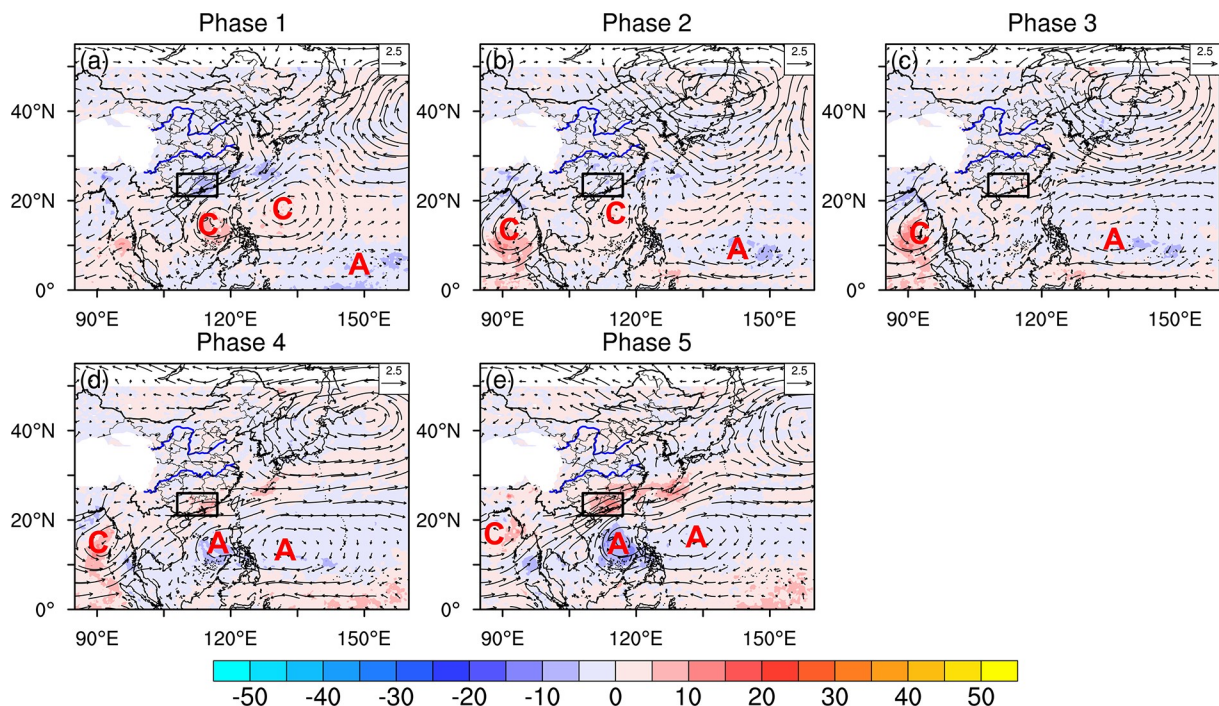

Fig. 9. As in Fig. 6 but for the 20–60-d bandpass-filtered disturbances and precipitation anomalies.

Despite both the unfiltered (raw) and low-frequency background circulation fields (> 60 d) being convergent on day −3 and day −2, the synoptic-scale disturbances nevertheless suppress the formation of heavy precipitation. From day −1, synoptic-scale disturbances become phase locked with low-frequency disturbances, and then EPEs occur with the strongest moisture convergence on day 0. In addition, the high-frequency disturbances (< 3 d) all contribute moisture convergence to different degrees on day 0, and the low-frequency background circulation exhibits relatively weak water vapor convergence during day −3 to day 0. It should be mentioned that the amounts of VIMFCs are not proportional to the total EPE intensity because the formation of EPEs is affected not only by the disturbances but also by the topographic conditions and other precipitation generation mechanisms.

Because the disturbances are most obvious in the lower troposphere, Table 6 gives the 850-hPa relative vorticity analysis to further illustrate the relative contributions of disturbances on each time scale. The results are similar as those of VIMFCs, i.e., the dominant disturbances in each type of EPEs make a major contribution to the increase of raw positive vorticity on peak wet day.

5. Summary and discussion

In this study, the major frequency modes of pre-summer-season EPEs over SC during 1998–2018 were examined. A total of 67 significant EPEs were identified based on the given criteria. Each EPE exhibited a prominent 3–8-d frequency band; however, the majority of EPEs over SC were characterized by multi-frequency bands, and the

amounts (percentage) of single 3–8-d synoptic scale, and 3–8-d & 10–20-d, 3–8-d & 15–40-d and 3–8-d & 20–60-d combined mode cases, were 25 (37%), 18 (27%), 15 (22%), and 9 (14%), respectively. Compared with the EPEs of the single synoptic mode, the peak precipitation intensities were larger (nearly 36.0 vs 33.5 mm d^{-1}) in the multiscale combined modes.

The low-level raw circulation fields were characterized by notable anomalously low-pressure systems over SC for all the EPEs, and the EPEs mainly occurred in the southeast quadrant of the cyclonic circulation or at the bottom of the deep trough where intense southwesterly flow dominated. Bandpass-filtered disturbances helped to reveal the direct precipitating systems, their area of origin, and life cycle. At the synoptic scale, almost all the precipitating disturbances originated from mid–high latitudes (troughs and anticyclonic anomalies in types I and IV) or downstream of the TP (anticyclonic–cyclonic wave trains in types II and III). The SC region was under the control of westerly–southwesterly–southerly flow on the peak wet day, and only a few cases were affected by the northeasterly flow of the Yellow–Huaihe Basin anticyclonic anomaly. At the QBW scale, the areas of origin of disturbances ranged from the tropical Pacific, downstream of the TP, to mid–high latitudes. The cyclonic–anticyclonic anomaly couplets in type I and type III propagated northwestwards and eastwards, respectively, and the extended trough in type II was the result of the mid–high latitude cyclonic anomaly strengthening and then merging with the cyclonic anomaly downstream of the TP. The disturbances at the QM scale were nearly the same as those in type I and type III of the QBW scale, except that the cyclonic–anticyclonic anomaly couplet east of the TP

Table 5. The unfiltered and bandpass-filtered area-averaged 1000–300-hPa VIMFC (vertically integrated moisture flux convergence; 10^{-6} kg m^{-2} s^{-1}) over SC for multiscale combined mode.

Multiscale combined mode	Frequency band	Day-3	Day-2	Day-1	Day0
Synoptic&QBW	HFD*	−3.95	−0.19	4.23	−4.42 (4%)
	Synoptic	26.7	31.68	**−15.55**	**−36.44 (35%)**
	QBW	**−13.42**	**−23.86**	**−30.03**	**−30.27 (29%)**
	ISO	−4.37	−6.94	−9.27	−11.22 (11%)
	LFBS*	−15.08	−15.13	−15.09	−14.95(14%)
	Unfiltered	−8.35	−15.91	−70.62	−104.08
Synoptic&QM	HFD	−0.59	−2.89	9.98	−15.72 (22%)
	Synoptic	17.05	15.05	**−11.06**	**−26.81 (38%)**
	QM	**−22.13**	**−28.34**	**−31.5**	**−31.12 (44%)**
	LFBS	−7.02	−7.06	−7.05	−6.98 (10%)
	Unfiltered	−10.37	−15.04	−28.13	−70.09
Synoptic&ISO	HFD	−6.78	−5.16	15.19	**−20.62 (23%)**
	Synoptic	2.06	37.63	**−5.52**	**−28.95 (32%)**
	QBW	−2.03	1.04	3.41	4.08 (−5%)
	ISO	**−29.57**	**−32.8**	**−34.38**	**−34.17 (38%)**
	LFBS	−4.53	−4.41	−4.23	−4.00(5%)
	Unfiltered	−45.17	−9.19	−31.38	−89.26

*HFD and LFBS refer to high-frequency disturbances (< 3 d) and low-frequency background circulation (> 60 d) components, respectively. Values in bold indicate significant positive contribution to EPEs.

Table 6. As in Table 5, but for the 850-hPa relative vorticity (10^{-6} s^{-1}).

Multiscale combined mode	Frequency band	Day-3	Day-2	Day-1	Day0
Synoptic&QBW	HFD	−0.89	0.96	−0.63	0.04 (0.3%)
	Synoptic	−0.82	−2.87	−0.94	**4.99 (43%)**
	QBW	−1.29	**0.42**	**2.2**	**3.58 (31%)**
	ISO	−0.44	−0.29	−0.1	0.11 (1%)
	LFBS	2.39	2.51	2.61	2.69 (23%)
	Unfiltered	−2.01	0.04	2.89	11.55
Synoptic&QM	HFD	0.07	−0.11	0.23	−0.49 (−6%)
	Synoptic	0.31	−3.14	−2.92	**3.53 (41%)**
	QM	0.65	**1.83**	**2.86**	**3.62 (42%)**
	LFBS	1.12	1.16	1.2	1.23 (14%)
	Unfiltered	2.16	0.32	2.19	8.54
Synoptic&ISO	HFD	0.18	−0.08	−0.16	0.52 (4%)
	Synoptic	1.11	−6.54	−3.62	**6.88 (53%)**
	QBW	0.7	0.87	0.8	0.52 (4%)
	ISO	**2.68**	**3.14**	**3.45**	**3.59 (28%)**
	LFBS	0.96	0.96	0.95	0.92 (7%)
	Unfiltered	5.13	−2.4	1.06	12.98

Note: values in bold indicate significant positive contribution to EPEs.

propagated southeastwards. The disturbances at the ISO scale were all confined to the tropical regions south of 20°N and consistently propagated westwards. The disturbances were stable, with very large scope, and they reflected well the precise process of expansion of the WPSH from phase 1.

Figure 10 is a schematic diagram of the areas of origin and propagation pathways of different scale disturbances. In short, the typical synoptic-scale disturbances all originate from mid–high latitudes or downstream of the TP (pathway 1 or 2). In contrast, the low-frequency ISO disturbances are confined to the tropical regions and influence SC by their marginal flows (pathway 3). The origins of QBW- and QM-scale disturbances vary from the tropics to mid–high latitudes (pathways 1, 2 or 3) and the cyclonic anomaly is usually the direct precipitating system. In the multiscale combined modes, all the low-frequency disturbances, such as a cyclonic anomaly, trough, as well as intense southwesterly flows, provide favorable background conditions for EPEs over SC. It is the synoptic disturbances that ultimately trigger EPEs on the peak wet day, which is well reflected by the area-averaged VIMFC and 850-hPa relative vorticity analysis using both raw and bandpass-filtered values.

The focus of this study was on investigating multi-frequency modes of EPEs longer than 3 days. It should be mentioned, however, that much higher frequency sub-synoptic and mesoscale disturbances, static topography, and even the urban heat island effect, may be quite important for the occurrence of EPEs over SC. As an extension to the findings in Huang et al. (2018), we reveal that most EPEs over SC have two dominant frequency modes and that multiscale combined actions enhance the peak precipitation intensity. Second, the QM scale is a non-ignorable frequency band over SC, in which the disturbances have similar propagation pathways as those on the QBW scale. Third, the disturbances at the syn-optic, QBW and QM scales all may originate from mid–high latitudes (except QM), downstream of the TP, and in the tropical western Pacific (or SCS) during the pre-summer season, instead of only in the tropical western Pacific as concluded in Li and Zhou (2015) for the boreal summer season (July–September). This means that predicting EPEs in the pre-summer season is more challenging, because the internal variability of mid–high latitude systems is greater and the predictability of models is poor.

In terms of the classification of synoptic-scale disturbances, the MV_EOF results were consistent with the subjective analysis and were reasonably robust even with variation of the target zone. However, for the low-frequency modes, the MV_EOF results were dependent on the choice of spatial domain, and we were unable to obtain a robust automated classification. Meanwhile, the fewer EPE cases in each frequency mode also limit the application of the objective classification method. As reviewed by Philipp et al. (2010), there is no absolute automatic weather and circulation classification method, and both objective and subjective classifications have their own advantages and disadvantages. The remaining issues regarding the multiscale combined actions of EPEs include how to further quantify the relative contributions of different temporal scale disturbances and what multiscale interactions evolve during EPEs. For example, to what extent will the precipitation intensity of EPEs be reduced if synoptic-scale or other low-frequency disturbances are removed from the raw circulation fields? If the synoptic-scale (low-frequency) disturbances are removed, what will happen to the low-frequency (synoptic-scale) disturbances? And what processes of interaction are at work among different scale disturbances? These issues will be further analyzed via numerical simulations and diagnostic analysis in future research.
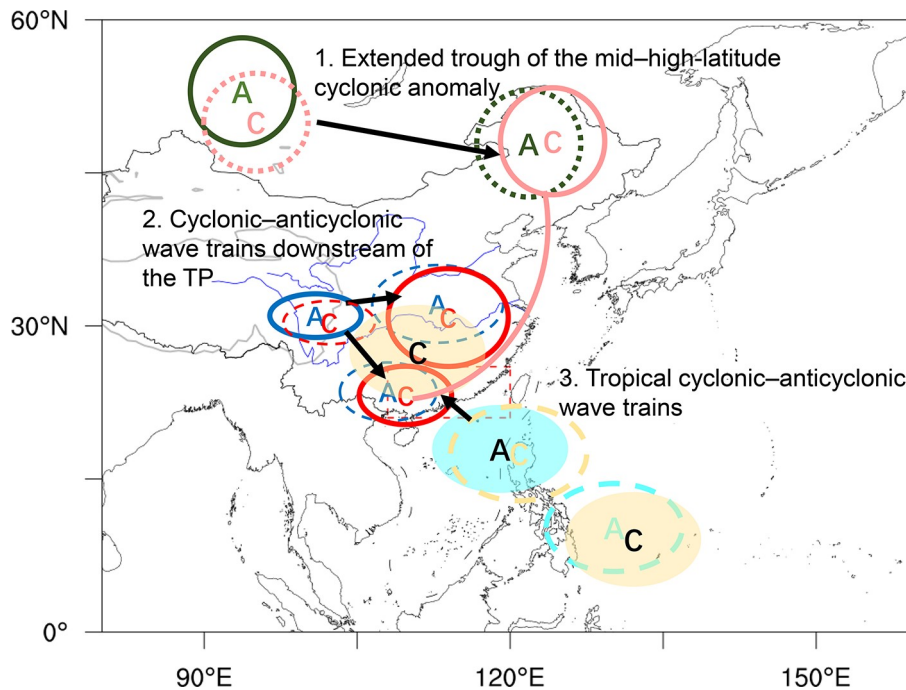
Fig. 10. Schematic diagram of the areas of origin and propagation pathways of different scale precipitating disturbances. "1" is the pathway of extended trough of the mid–high-latitude cyclonic anomaly (type I in 3–8-d, II in 10–20-d); "2" is the pathways for northeastward and southeastward propagating cyclonic–anticyclonic wave trains downstream of the TP (types II, III in 3–8-d; III in 10–20-d; II in 15–40-d); "3" is the pathway of tropical cyclonic–anticyclonic wave trains (type I in 10–20-d and 15–40-d; 20–60-d). Solid (dashed) circles represent the position of cyclonic and anticyclonic disturbances on the peak wet (dry) phase. The northwest-southeastward cyclonic–anticyclonic–cyclonic wave train is indicated by shallow yellow. Blue shading in pathway "3" corresponds to the disturbances on peak wet phase of type I in 10–20-d and 15–40-d oscillation. The cyclonic/anticyclonic disturbances with dashed circles (shading circles) represent peak dry (wet) phase of 20–60-d oscillation. Note that type IV of synoptic-scale disturbances is not shown.

REFERENCES

Bao, M., 2007: The statistical analysis of the persistent heavy rain in the last 50 years over China and their backgrounds on the large scale circulation. *Chinese Journal of Atmospheric Science*, **31**, 779−792, https://doi.org/10.3878/j.issn.1006-9895.2007.05.03. (in Chinese with English abstract)

Cao, X., X. J. Ren, X. Q. Yang, and J. B. Fang, 2012: The quasi-biweekly oscillation characteristics of persistent severe rain and its general circulation anomaly over southeast China from May to August. *Acta Meteorologica Sinica*, **70**, 766−778, https://doi.org/10.11676/qxxb2012.062. (in Chinese with English abstract)

Chen, G. H., and C.-H. Sui, 2010: Characteristics and origin of quasi-biweekly oscillation over the western North Pacific during boreal summer. *J. Geophys. Res.*, **115**, D14113, https://doi.org/10.1029/2009JD013389.

Chen, M. Y., W. Shi, P. P. Xie, V. B. S. Silva, V. E. Kousky, R. W. Higgins, and J. E. Janowiak, 2008: Assessing objective techniques for gauge-based analyses of global daily precipitation. *J. Geophys. Res.*, 2008, **113**, D04110, https://doi.org/10.1029/2007JD009132.

Chen, X. C., F. Q. Zhang, and K. Zhao, 2016: Diurnal variations of the land-sea breeze and its related precipitation over South China. *J. Atmos. Sci.*, **73**, 4793−4815, https://doi.org/10.1175/JAS-D-16-0106.1.

Chen, Y., and P. M. Zhai, 2013: Persistent extreme precipitation events in China during 1951−2010. *Climate Research*, **57**, 143−155, https://doi.org/10.3354/cr01171.

Dee, D. P., and Coauthors, 2011: The ERA-Interim reanalysis: Configuration and performance of the data assimilation system.

Quart. J. Roy. Meteor. Soc., **137**, 553−597, https://doi.org/10.1002/qj.828.

Ding, Y. H., 2005: *Advanced Synoptic Meteorology*. 2nd ed., China Meteorological Press, 583 pp. (in Chinese)

Ding, Y. H., 2019: The major advances and development process of the theory of heavy rainfalls in China. *Torrential Rain and Disasters*, **38**, 395−406, https://doi.org/10.3969/j.issn.1004-9045.2019.05.001. (in Chinese with English abstract)

Du, Y., and G. X. Chen, 2019a: Climatology of low-level jets and their impact on rainfall over southern China during the early-summer rainy season. *J. Climate*, **32**, 8813−8833, https://doi.org/10.1175/JCLI-D-19-0306.1.

Du, Y., and G. X. Chen, 2019b: Heavy rainfall associated with double low-level jets over Southern China. Part II: Convection initiation. *Mon. Wea. Rev.*, **147**, 543−565, https://doi.org/10.1175/MWR-D-18-0102.1.

Du, Y., G. X. Chen, B. Han, C. Y. Mai, L. Q. Bai, and M. H. Li, 2020a: Convection initiation and growth at the coast of South China. Part I: Effect of the marine boundary layer jet. *Mon. Wea. Rev.*, **148**, 3847−3869, https://doi.org/10.1175/MWR-D-20-0089.1.

Du, Y., G. X. Chen, B. Han, L. Q. Bai, and M. H. Li, 2020b: Convection initiation and growth at the coast of South China. Part II: Effects of the terrain, coastline, and cold pools. *Mon. Wea. Rev*, **148**, 3871−3892, https://doi.org/10.1175/MWR-D-20-0090.1.

Gao, M. N., J. Yang, B. Wang, S. Y. Zhou, D. Y. Gong, and S.-J. Kim, 2018: How are heat waves over Yangtze River valley associated with atmospheric quasi-biweekly oscillation. *Climate Dyn.*, **51**, 4421−4437, https://doi.org/10.1007/s00382-017-3526-z.

Gao, Z. B., J. S. Zhu, Y. Guo, N. Luo, Y. Fu, and T. T. Wang, 2021: Impact of land surface processes on a record-breaking rainfall event on May 06–07, 2017, in Guangzhou, China. *J. Geophys. Res.*, **126**, e2020JD032997, https://doi.org/10.1029/2020JD032997.

Gu, D. J., Z. P. Ji, X. R. Gao, G. F. Sun, and J. G. Xie, 2013: The relationship between the rainfall during the annually first rainy season in Guangdong and the quasi-biweekly oscillation of wind field in the north of South China Sea. *Journal of Tropical Meteorology*, **29**, 189−197, https://doi.org/10.3969/j.issn.1004-4965.2013.02.002. (in Chinese with English abstract)

He, L. F., T. Chen, and Q. Kong, 2016: A review of studies on pre-frontal torrential rain in South China. *Journal of Applied Meteorological Science*, **27**, 559−569, https://doi.org/10.11898/1001-7313.20160505. (in Chinese with English abstract)

Hong, W., and X. J. Ren, 2013: Persistent heavy rainfall over South China during May-August: Subseasonal anomalies of circulation and sea surface temperature. *Acta Meteorologica Sinica*, **27**, 769−787, https://doi.org/10.1007/s13351-013-0607-8.

Huang, L., Y. L. Luo, and D.-L. Zhang, 2018: The relationship between anomalous presummer extreme rainfall over South China and synoptic disturbances. *J. Geophys. Res.*, **123**, 3395−3413, https://doi.org/10.1002/2017JD028106.

Huang, Y. J., Y. B. Liu, Y. W. Liu, H. Y. Li, and J. C. Knievel, 2019: Mechanisms for a record-breaking rainfall in the coastal metropolitan city of Guangzhou, China: Observation analysis and nested very large eddy simulation with the WRF model. *J. Geophys. Res.*, **124**, 1370−1391, https://doi.org/10.1029/2018JD029668.

Huffman, G. J., and D. T. Bolvin, 2018: TRMM and other data precipitation data set documentation. [Available online from https://docserver.gesdisc.eosdis.nasa.gov/public/project/GPM/3B42_3B43_doc_V7.pdf]

Huffman, G J., R. F. Adler, D. T. Bolvin, and E. J. Nelkin. 2010: The TRMM multi-satellite precipitation analysis (TMPA). *Satellite Rainfall Applications for Surface Hydrology*, M. Gebremichael and F. Hossain, Eds., Springer, 3−22, https://doi.org/10.1007/978-90-481-2915-7_1.

Huffman, G. J., D. T. Bolvin, E. J. Nelkin, and R. F. Adler, 2016: TRMM (TMPA) Precipitation L3 1 day 0.25 degree x 0.25 degree V7. A. Savtchenko, Ed., Goddard Earth Sciences Data and Information Services Center (GES DISC). [Available online from https://disc.gsfc.nasa.gov/datasets/TRMM_3B42_Daily_7/summary]

Jiang, Z. N, D.-L. Zhang, and H. B. Liu, 2020: Roles of synoptic to quasi-monthly disturbances in generating two pre-summer heavy rainfall episodes over South China. *Adv. Atmos. Sci.*, **37**, 211−228, https://doi.org/10.1007/s00376-019-8156-4.

Jiang, Z. N., D.-L. Zhang, R. D. Xia, and T. T. Qian, 2017: Diurnal variations of presummer rainfall over southern China. *J. Climate*, **30**, 755−773, https://doi.org/10.1175/JCLI-D-15-0666.1.

Joyce, R. J., J. E. Janowiak, P. A. Arkin, and P. P. Xie, 2004: CMORPH: A method that produces global precipitation estimates from passive microwave and infrared data at high spatial and temporal resolution. *Journal of Hydrometeorology*, **5**, 487−503, https://doi.org/10.1175/1525-7541(2004)005<0487:CAMTPG>2.0.CO;2.

Li, C. H., T. M. Li, A. L. Lin, D. J. Gu, and B. Zheng, 2015: Relationship between summer rainfall anomalies and sub-seasonal oscillations in South China. *Climate Dyn.*, **44**, 423−439, https://doi.org/10.1007/s00382-014-2172-y.

Li, R. C. Y., and W. Zhou, 2015: Multiscale control of summertime persistent heavy precipitation events over South China in association with synoptic, intraseasonal, and low-frequency background. *Climate Dyn.*, **45**, 1043−1057, https://doi.org/10.1007/s00382-014-2347-6.

Liu, H. B., J. Yang, D.-L. Zhang, and B. Wang, 2014: Roles of synoptic to quasi-biweekly disturbances in generating the Summer 2003 heavy rainfall in East China. *Mon. Wea. Rev.*, **142**, 886−904, https://doi.org/10.1175/MWR-D-13-00055.1.

Liu, R. X., J. H. Sun, J. Wei, and S. M. Fu, 2016: Classification of persistent heavy rainfall events over South China and associated moisture source analysis. *J. Meteor. Res.*, **30**, 678−693, https://doi.org/10.1007/s13351-016-6042-x.

Luo, Y. L., R. D. Xia, and J. C. L. Chan, 2020: Characteristics, physical mechanisms, and prediction of pre-summer rainfall over South China: Research progress during 2008-2019. *J. Meteor. Soc. Japan*, **98**, 19−42, https://doi.org/10.2151/jmsj.2020-002.

Luo, Y. L., and Coauthors, 2017: The Southern China monsoon rainfall experiment (SCMREX). *Bull. Amer. Meteor. Soc.*, **98**, 999−1013, https://doi.org/10.1175/BAMS-D-15-00235.1 .

Mao, J. Y., and G. X. Wu, 2006: Intraseasonal variations of the Yangtze rainfall and its related atmospheric circulation features during the 1991 summer. *Climate Dyn.*, **27**, 815−830, https://doi.org/10.1007/s00382-006-0164-2.

Mao, J. Y., and J. C. L. Chan, 2005: Intraseasonal variability of the South China Sea summer monsoon. *J. Climate*, **18**, 2388−2402, https://doi.org/10.1175/JCLI3395.1.

Miao, R., M. Wen, R. H. Zhang, and L. Li, 2019: The influence of wave trains in mid-high latitudes on persistent heavy rain during the first rainy season over South China. *Climate Dyn.*, **53**, 2949−2968, https://doi.org/10.1007/s00382-019-04670-y.

Pan, W. J., J. Y. Mao, and G. X. Wu, 2013: Characteristics and Mechanism of the 10–20-Day oscillation of spring rainfall over southern China. *J. Climate*, **26**, 5072−5087, https://doi.org/10.1175/JCLI-D-12-00618.1.

Philipp, A., and Coauthors, 2010: Cost733cat–A database of weather and circulation type classifications. *Physics and Chemistry of the Earth, Parts A/B/C*, **35**, 360−373, https://doi.org/10.1016/j.pce.2009.12.010.

Tabari, H., 2020: Climate change impact on flood and extreme precipitation increases with water availability. *Scientific Reports*, **10**, 13768, https://doi.org/10.1038/s41598-020-70816-2.

Tang, T. Y., C.-S. Wu, A.-Y. Wang, E.-B. Hou, and H.-B. Luo, 2007: An observational study of interaseasonal variations over Guangdong Province China during the rainy season of 1999. *Journal of Tropical Meteorology*, **23**, 683−689, https://doi.org/10.3969/j.issn.1004-4965.2007.06.025. (in Chinese with English abstract)

Wang, B., 1992: The vertical structure and development of the ENSO anomaly mode during 1979−1989. *Journal of the Atmospheric Sciences*, **49**, 698−712, https://doi.org/10.1175/1520-0469(1992)049<0698:TVSADO>2.0.CO;2.

Wang, H. J., J. H. Sun, S. X. Zhao, and J. Wei, 2016: The multiscale factors favorable for a persistent heavy rain event over Hainan Island in October 2010. *Journal of Meteorological Research*, **30**, 496−512, https://doi.org/10.1007/s13351-016-6005-2.

Wang, X., and G. J. Zhang, 2019: Evaluation of the quasi-biweekly oscillation over the South China Sea in early and late summer in CAM5. *J. Climate*, **32**, 69−84, https://doi.org/10.1175/JCLI-D-18-0072.1.

Wu, M. W., Y. L. Luo, F. Chen, and W. K. Wong, 2019: Observed link of extreme hourly precipitation changes to urbanization over coastal South China. *J. Appl. Meteor. Climatol.*, **58**, 1799−1819, https://doi.org/10.1175/JAMC-D-18-0284.1.

Xie, P. P., R. Joyce, S. R. Wu, S. H. Yoo, Y. Yarosh, F. Y. Sun, and R. Lin, 2017: Reprocessed, bias-corrected CMORPH global high-resolution precipitation estimates from 1998. *Journal of Hydrometeorology*, **18**, 1617−1641, https://doi.org/10.1175/JHM-D-16-0168.1.

Yang, J., B. Wang, B. Wang, and Q. Bao, 2010: Biweekly and 21-30-day variations of the subtropical summer monsoon rainfall over the lower reach of the Yangtze River Basin. *J. Climate*, **23**, 1146−1159, https://doi.org/10.1175/2009jcli3005.1.

Yin, J. F., D. L. Zhang, Y. L. Luo, and R. Y. Ma, 2020: On the extreme rainfall event of 7 May 2017 over the coastal city of Guangzhou. Part I: Impacts of urbanization and orography. *Mon. Wea. Rev.*, **148**, 955−979, https://doi.org/10.1175/MWR-D-19-0212.1.

Zhang, C., X. G. Huang, J. F. Fei, X. Luo, and Y. Zhou, 2021: Spatiotemporal characteristics and associated synoptic patterns of extremely persistent heavy rainfall in Southern China. *J. Geophys. Res.*, **126**, e2020JD033253, https://doi.org/10.1029/2020JD033253.

Zhang, Y. C., J. H. Sun, and S. M. Fu, 2017: Main energy paths and energy cascade processes of the two types of persistent heavy rainfall events over the Yangtze River-Huaihe River Basin. *Adv. Atmos. Sci.*, **34**, 129−143, https://doi.org/10.1007/s00376-016-6117-8.

Zhou, W., and J. C. L. Chan, 2005: Intraseasonal oscillations and the South China Sea summer monsoon onset. *International Journal of Climatology*, **25**, 1585−1609, https://doi.org/10.1002/joc.1209.